

1 **Earth's radiation belts ions: patterns of the spatial-energy structure**  
2 **and its solar-cyclic variations**

3 **Alexander S. Kovtyukh**

4 Skobeltsyn Institute of Nuclear Physics, Moscow State University, Moscow, 119234, Russia;  
5 kovtyukhas@mail.ru

6 **Abstract** Spatial-energy distributions of the stationary fluxes of protons, helium and ions of  
7 carbon-nitrogen-oxygen (CNO) group, with energy from  $E \sim 100$  keV to 200 MeV, in the  
8 Earth's radiation belts (ERB), at  $L \sim 1-8$ , are considered here using data from satellites in the  
9 period 1961–2017. It has been found that the results of these measurements line up in the space  
10  $\{E, L\}$  following some regular patterns. Solar-cyclic (11-year) variations in the distributions of  
11 protons, helium and CNO group ions fluxes in the ERB are studied. It has been observed that in  
12 the inner regions of the ERB, fluxes decrease with increasing solar activity and that the solar-  
13 cyclic variations of fluxes of  $Z \geq 2$  ions are much greater than for protons; moreover, it seems  
14 that they increase with increasing atomic number  $Z$ . Finally, the possible physical mechanisms  
15 leading to formation of this spatial-energy structure and to the solar-cyclic variations of the  
16 ERB ion fluxes are discussed.

17  
18 **Keywords.** Magnetospheric physics (energetic particles, trapped). Radiation belts.  
19

## 20 1 Introduction

21 The ERB consist mainly of charged particles with energy from  $E \sim 100$  keV to several hundreds of  
22 megaelectronvolt (MeV). These particles are trapped by the geomagnetic field at altitudes from  $\sim$   
23 200 kilometers to  $\sim 50\text{--}70$  thousands kilometers. The ERB consist mainly of electrons and  
24 protons, but there are also helium nuclei and other  $Z > 2$  ions (like oxygen etc), where  $Z$  is the  
25 charge of the atomic nucleus with respect to the charge of the proton. During geomagnetic  
26 disturbances, ion fluxes, and their distributions are changed. These fluxes depend also on the phase  
27 of the solar cycle, conditions in the interplanetary space, and other factors.

28 Particles with different energy  $E$  and pitch angles  $\alpha$  ( $\alpha$  is the angle between a the local vector of  
29 the magnetic field and the vector of a particle velocity), which are injected into some point of the  
30 geomagnetic trap, drift conserving the adiabatic invariants ( $\mu$ ,  $K$ ,  $\Phi$ ) and populate a narrow layer  
31 surrounding the Earth (Alfvén and Fälthammar, 1963; Northrop, 1963). This layer is called the  
32 drift shell. Therefore, experimental data on the ERB are often represented in coordinates  $\{L, B\}$ ,  
33 where  $L$  is the drift shell parameter and  $B$  is the local induction of the magnetic field (McIlwain,  
34 1961). For the dipole magnetic field,  $L$  is a distance, in the equatorial plane, from the given  
35 magnetic field line to the center of the dipole itself (in Earth's radii  $R_E$ ).

36 The stationary fluxes  $J$  of the ERB particles with given energy and pitch angle  $\alpha$  decrease  
37 usually when the point of observation is shifted from the equatorial plane to higher latitudes along  
38 a certain magnetic field line (if we exclude the peripheral regions of the geomagnetic trap, where  
39 the drift shells of the captured particles are split and branched). This dependence is described by  
40 the functions  $J(B/B_0)$ , where  $B$  and  $B_0$  are values of the magnetic field at the point of observation  
41 and in the equatorial plane on the same magnetic field line, respectively.

42 Outer and inner regions of the ERB are maintained in dynamic equilibrium with the  
43 environment by different mechanisms (see review Kovtyukh, 2018).

44 The outer belt ( $L > 3.5$ ) is formed mainly by the mechanisms of radial diffusion of ions towards  
45 the Earth under the action of fluctuations of both electric and magnetic fields resonating with their  
46 drift periods. This transport is accompanied by the betatron acceleration and by the ionization  
47 losses of the ions as a result of their interactions with the plasmasphere and with residual  
48 atmosphere.

49 The inner belt ( $L < 2.5$ ) of protons with  $E > 10$  MeV is formed ~~by~~ mainly as a result of decay of  
50 neutrons knocked from the nuclei of the atmospheric atoms by the Galactic Cosmic Rays. For  
51 protons with  $E < 10$  MeV this, mechanism (CRAND) is supplemented by the radial diffusion of  
52 particles from the outer to the inner belt. The inner belt of ions with  $Z > 4$  is formed mainly from  
53 the ions of the Anomalous component of Cosmic Rays.

54 In the intermediate region ( $2.5 < L < 3.5$ ), ~~the mechanism is operated also the mechanism~~ of a  
55 ion capture from Solar Cosmic Rays takes place during strong magnetic storms (see, e.g.,  
56 Selesnick et al., 2014).

57 Thus, the main mechanisms of formation of the ERB, together with the sources of injection and  
58 losses of ions, are known. However, for a comprehensive verification of the physical models and to  
59 identify the mathematical models and their parameters, the formulation of complete and reliable  
60 empirical ~~models~~ **representations** of the ERB for each of the ion components, is necessary; it is  
61 also necessary for ensuring the safety of space flights.

62 These models can be created only using experimental data, obtained over many years and  
63 decades; such models (see, e.g., Ginet et al., 2013) were already created for protons (AP8/AP9)  
64 and they are widely used in space research. On the contrary, measurements of  $Z \geq 2$  ion fluxes  
65 suffer from technical problems due to small statistics and high background of protons and  
66 electrons. For this reasons, empirical and semi-empirical models for  $Z \geq 2$  ions, are applicable  
67 only to very limited regions of the space  $\{E, L\}$ .

68 One of the main problems of this work is to consider the possibility to create a sufficiently  
69 complete and reliable empirical models of the ERB for these ions based on currently available  
70 experimental data.

71 In the following sections, the spatial-energy structure of the ERB in the  $\{E, L\}$  space for  
72 protons, helium and CNO group ions are considered (Sect. 2) together with possible physical  
73 mechanisms of formation of these structures and their solar-cyclic variations (Sect. 3). Finally, the  
74 main conclusions of this work are given (Sect. 4).

## 75 2 Spatial-energy distributions of the ion fluxes near the equatorial plane

76 There can be ions trapped in drift shells only with energies less than some maximum values,  
77 determined by the Alfvén's criterion:  $\rho_i(L, E, M_i, Q_i) \ll R_c(L)$ , where  $\rho_i$  is the gyroradius of ions,  
78 and  $R_c$  is the radius of curvature of the magnetic field near the equatorial plane ( $M_i$  and  $Q_i$  are mass  
79 and charge of ions with respect to the corresponding values for protons). According to this  
80 criterion and to the theory of stochastic motion of particles, the geomagnetic trap can capture and  
81 durably hold only ions with  $E$  (MeV)  $< 2000 \times (Q_i^2/M_i) L^{-4}$  (Ilyin et al., 1984). The green line in  
82 Figs 1-6 represents this very boundary.

83 When comparing the data of various experiments in the ERB, the question arises about the  
84 compatibility of these results with each other and the reasons for their discrepancies. A significant  
85 number of these discrepancies can be connected to the differences in their trajectories; in the  
86 construction of the instruments and their angular characteristics; in the energy ranges and sets of  
87 energy channels. For the stationary ERB, these discrepancies can also be associated with  
88 differences in the general state of the Sun, heliosphere and magnetosphere of the Earth during  
89 various periods of data-taking. These factors influence the fluxes of ions with  $Z \geq 2$  in the ERB  
90 more significantly with respect to proton fluxes (see, e.g., Kovtyukh, 2018).

91 In this section, experimental data of various satellites, which were obtained for quiet periods  
92 ( $Kp < 2$ ) and near the equatorial plane of the ERB for ions with equatorial pitch angles  $\alpha_0 \approx 90^\circ$   
93 have been used. In the regions of  $E$  and  $L$  shells, where these data were obtained, the ion fluxes are  
94 not distorted by the background of other particles.

95 In many important experiments, the instruments were not able to separate fluxes of ions by their  
96 charge. Moreover, for the ions of the CNO group, the separation by mass are not usually  
97 performed. For heavier species, for example for Fe ions, we have very small data-sets. Therefore,  
98 this work presents data on helium ions (without any charge separating) and CNO ions (without any  
99 mass or charge separation).

100 To solve the aforementioned problems, it is important to choose the form of representation  
101 (space of variables), in which the results of every experiment can be compared to the others. In our  
102 case, the space  $\{E, L\}$  has been used; this choice is very efficient to better organize fragmentary  
103 experimental data obtained in different ranges of  $E$  and  $L$ .

104 Figures 1–6 show the spatial-energy distributions of the fluxes of protons, helium ions, and ions  
105 of the CNO group near the equatorial plane. Odd figures refer to periods near the minima, and  
106 even figures refer to periods near the solar activity maxima. The values  $E$  and  $L$  in these figures are  
107 presented in logarithmic scales. Statistical and methodical errors of the experimental points on  
108 these figures do not exceed of the size of these points. The markers are connected by lines of equal  
109 intensity of ion fluxes (iso-lines); the decimal logarithms of the fluxes  $J$ , in unit of  $(\text{cm}^2 \text{ s ster}$   
110  $\text{MeV/n})^{-1}$ , are shown near each iso-lines.

111 Such representations of the experimental data are not only visual, but also very convenient and  
112 rather universal. Obviously, Figs. 1–6 actually show both radial profiles of the fluxes of ions for a  
113 given energy and ion energy spectra for a given  $L$  shell.

114 The points in Figs. 1–6 have been obtained from the radial profiles of fluxes  $J(L)$  for the  
115 average energies of the ions in the channels of the instruments. Unlike electron fluxes or ion fluxes

116 measured during geo-active conditions, the ion fluxes considered here (i.e. during quiet periods),  
117 ~~for ions usually~~ have only one maximum in the functions  $J(L)$ . As a result, for each experiment, 1  
118 or 2 points were obtained (on the outer and inner edges of these profiles) with certain values of  $E$   
119 and  $L$  for a given level of ion fluxes. Sometimes, especially for fluxes, only one point was  
120 obtained: in these cases, the radial profile of the ion fluxes was cutoff at small values of  $L$  due to a  
121 significant background of contaminating particles and no interpolation/extrapolation has been  
122 performed whatsoever.

123 Each iso-line, shown in these figures, has been evaluated separately from the corresponding set  
124 of experimental points (icons); then it was transferred (along with the icons) to the corresponding  
125 figure; thus, in more abundantly populated sectors of the plots (i.e. for protons with  $E > 1$  MeV at  
126  $L > 2$ ) such iso-lines are mixing in Figs. 1–2. In case of a large distance between neighboring  
127 points, the corresponding segments of the iso-lines are shown as dashed arcs.

128 The radial profiles of the differential fluxes  $J(L)$  of particles with different energy tend to  
129 intersect with each other in those regions where the energy spectra present some local maximum or  
130 minimum. On the contrary, the iso-lines cannot intersect with each other: because this would mean  
131 that, at the same point in the space  $\{E, L\}$ , the ion fluxes differ very significantly (by an order of  
132 magnitude). Such uncertainty does not have a physical sense and a special analysis is needed to  
133 identify other possible sources of errors.

134 Representing plots in a different space of variables would lead only to more significant  
135 methodological errors and uncertainties, because of the natural differences in the instrumentation  
136 of the experiments taken into account; thus, a series of approximations or  
137 interpolation/extrapolation techniques would become inevitable.

## 138 **2.1 Spatial-energy structure of the proton fluxes**

139 There is a large number of experimental data concerning ERB protons; the most important of them  
140 are presented in Figs. 1 and 2. These figures serve as a comparison with similar distributions of  $Z \geq$   
141 2 ions (Figs. 3–6).

142 Figure 1 sums up results from the satellites Relay-1 (Freden et al., 1965); Ohzora or EXIS C:  
143 Exospheric Satellite C, Akebono or EXOS-D: Exospheric Satellite D and ETS-VI: Engineering Test  
144 Satellite (Goka et al., 1999). These results have been collected during minimum periods of various  
145 solar cycles, i.e. between 19<sup>th</sup> / 20<sup>th</sup> (1963), 21<sup>th</sup> / 22<sup>th</sup> (1984–1985), and 22<sup>th</sup> / 23<sup>th</sup> (1994–1996) of  
146 the solar activity cycles.

147 Figure 2 sums up results from the satellites 1968-81A (Stevens et al., 1970), Injun-5 or  
148 Explorer-40 (Krimigis, 1970; Venkatesan and Krimigis, 1971; Pizzella and Randall, 1971), 1969-  
149 025C or OV1-19: Orbiting Vehicle 1-19 (Croley et al., 1976), Azur or GRS A: German Research  
150 Satellite A (Hovestadt et al., 1972; Westphalen and Spjeldvik, 1982), Molniya-1 (Panasyuk and  
151 Sosnovets, 1973), GEOS-2: Geodetic Earth Orbiting Satellite 2 (Wilken et al., 1986), CRRES: The  
152 Combined Release and Radiation Effects Satellite (Albert et al., 1998; Vacaresse et al., 1999), GEO-  
153 3: Geostationary Orbit 3 (Selesnick et al., 2010) and Van Allen Probes (Selesnick et al., 2014,  
154 2018). These results were obtained during maximum periods of 20<sup>th</sup> (1968–1971), 22<sup>th</sup> (1990–  
155 1991), 23<sup>th</sup> (2000), and 24<sup>th</sup> (2012–2017) solar cycles.

156 The data of the satellites Explorer-45 (Fritz and Spjeldvik, 1979, 1981) and ISEE-1:  
157 International Sun-Earth Explorer 1 or Explorer-56 (Williams, 1981; Williams and Frank, 1984) are  
158 given in both Figs. 1 and 2 because solar-cyclic variations of the ERB proton fluxes are negligible  
159 at  $L > 2.5$  (see, e.g., Vacaresse et al., 1999).

160 From a comparison of Figs. 1 and 2, one can see that at  $L < 2.5$  (especially at  $L < 1.4$ ) the proton  
161 fluxes during solar minima (Fig. 1) are higher than during maxima (Fig. 2). In addition, in the  
162 former the inner edge of the proton belt is less steep and it can reach smaller  $L$  shells (for  $E > 1$   
163 MeV). The distributions of protons in the space  $\{\mu, L\}$  (see, e.g., Kovtyukh,(2016a,b) , which I  
164 have been constructed from Figs. 1 and 2 confirm these conclusions.

165 In Figs. 1 and 2, the iso-lines of proton fluxes are almost parallel to each other on  $L > 3$  at  
 166 sufficiently high energies. Since these iso-lines have separated from each other by approximately  
 167 equal intervals on a logarithmic scale of the energy, this region in the space  $\{E, L\}$  corresponds to  
 168 power-law spectra of the ERB protons: for power-law spectra,  $J \propto E^{-\gamma}$ , where the index  $\gamma = -$   
 169  $\Delta(\log J)/\Delta(\log E)$ . In these figures, this region is located between the green and red lines.

170 The red line corresponds to the lower boundary ( $E_b$ ) of the power-law tail of the proton spectra.  
 171 For this line,  $E_b \sim 36 \times L^{-3}$  MeV. Some changes in the slope of these iso-lines at  $L > 6$  can be  
 172 connected to a discrepancy between the real configuration of the magnetic field lines and the  
 173 dipolar configuration (used here for  $L$  shells calculation).

174 For the dipole magnetic field region, the points on the red line correspond to particles with a  
 175 specific value of the 1<sup>st</sup> adiabatic invariant of motion ( $\mu_b$ ). For Figs. 1 and 2, the average value  $\mu_b$   
 176 is  $\sim 1.16$  keV nT<sup>-1</sup>. Segments of an iso-lines, that are parallel to the red line, also correspond to  
 177 certain values of the invariant  $\mu$ . In this region of the space  $\{E, L\}$  the ionization and other losses  
 178 of the ERB protons during radial drift can be neglected, and changes of fluxes with changing  $L$  are  
 179 practically reduced to adiabatic transformations in a magnetic field.

180 It results from these figures that at  $L = 3-6$ , the value  $\gamma = 4.8 \pm 0.5$ . At  $L > 6$  the distances  
 181 between these iso-lines increase with  $L$ , and the value  $\gamma$  is decreased from  $\sim 4.7-5.0$  at  $L = 6$  to  $\sim$   
 182  $4.1-4.5$  at  $L = 8$ . This is due to the deviation of the magnetic field from the dipole configuration as  
 183 well as to the increasing variability of this field with increasing  $L$ .

184 According to the data of satellites considered in (Kovtyukh, 2001), invariant parameters  $\mu_b$  and  $\gamma$   
 185 were found only at  $L > 3$ . In this work, a wider range of  $L$  and  $E$  is considered, and for protons with  
 186  $E > 10$  MeV these parameters can be traced to  $L \sim 2$ . At  $L = 2$ ,  $\gamma = 4.4 \pm 0.6$  (Fig. 1) and  $\gamma = 4.7 \pm 1.3$   
 187 (Fig. 2). This is due to the fact that the energy range is significantly extended toward higher values  
 188 (up to 200 MeV), but here the ionization losses for protons rapidly decrease (see, e.g., Schulz and  
 189 Lanzerotti, 1974; Kovtyukh, 2016a).

## 190 2.2 Spatial-energy structure of the helium ion fluxes

191 In Figs. 3 and 4 helium ion fluxes, averaged for quiet periods ( $Kp < 2$ ), are presented.

192 Figure 3 sums up results from the satellites Molnija-2 (Panasyuk et al., 1977), Prognoz-5  
 193 (Lutsenko and Nikolaeva, 1978), ISEE-1: The International Sun-Earth Explorer 1 (Hovestadt et al.,  
 194 1981); Akebono or EXOS-D: Exospheric Satellite D and ETS-VI: Engineering Test Satellite (Goka et  
 195 al., 1999). These results have been collected during minimum periods of various solar cycles, i.e.  
 196 between 20<sup>th</sup> / 21<sup>th</sup> (1975–1977), 21<sup>th</sup> / 22<sup>th</sup> (1984–1985), and 22<sup>th</sup> / 23<sup>th</sup> (1994–1996) of the solar  
 197 activity cycles.

198 Figure 4 sums up results from the satellites OV1-19: Orbiting Vehicle 1-19 (Blake et al., 1973;  
 199 Fennell and Blake, 1976), Explorer-45 (Fritz and Spjeldvik, 1978, 1979; Spjeldvik and Fritz,  
 200 1981), SCATHA: Spacecraft Charging At High Altitudes (Blake and Fennell, 1981; Chenette et al.,  
 201 1984). These results were obtained during maximum periods of 20<sup>th</sup> (1968–1971) and 21<sup>th</sup> (1979)  
 202 solar cycles.

203 From a comparison of Figs. 1–2 with Figs. 3–4, one can see that at  $L > 2$  for helium ions the  
 204 solar-cyclic (11-year) variations are greater than for protons. For example, at  $L \sim 2-3$  from  
 205 maximum to minimum of solar activity fluxes of protons with  $E > 1$  MeV practically do not  
 206 change, and the fluxes of helium ions with  $E > 1$  MeV/n are increased by one order of magnitude.

207 Figures 3 and 4 show the same patterns as for protons, but the distribution of helium ion fluxes  
 208 is slightly shifted towards higher values of  $L$  shell (with respect to protons). Unlike protons, there  
 209 are significant “white spots” in these figures: because there are no experimental data for helium  
 210 ions in these regions.

211 The red line on these figures corresponds to the lower boundary of the power-law tail of the  
 212 helium ions spectra. For this line,  $E_b/M_i \sim 43.4 \times L^{-3}$  MeV/n (Fig. 3) and  $E_b/M_i \sim 21.7 \times L^{-3}$  MeV/n

213 (Fig. 4). If one takes into account that at  $L < 6$  for helium ions with  $E > 0.2$  MeV/n the average  
 214 charge  $Q_i = +2$  (see, e.g., Spjeldvik, 1979), then for the considered boundary we get:  $\mu_b \sim 1.4 \times Q_i$   
 215 keV/n $\times$ nT $^{-1}$  at the maximum of solar activity and  $\mu_b \sim 1.4 \times M_i$  keV/n $\times$ nT $^{-1}$  at the minimum of solar  
 216 activity (for the dipole magnetic field region). The iso-lines of helium ion fluxes in Figs. 3 and 4,  
 217 which pass above the red line at  $L > 2.5$ , correspond to an average value of  $\gamma \sim 5.5$ .

218 For helium spectra, as for protons ones, the values of the parameters of the power-law tail are in  
 219 good agreement with what has been found in (Kovtyukh, 2001).

220 At the same time, one can see that the iso-lines of the fluxes of helium ions in the region above  
 221 the red line (i.e. in the region of power-law spectra) substantially deviate from the slope of the red  
 222 line. At  $L > 3$  the fluxes of helium ions with given energy are increase with decreasing  $L$  slower  
 223 than expected from adiabatic transformation (see Kovtyukh, 2001). This means that the ionization  
 224 losses of the ERB helium ions significantly exceed these losses for protons, in agreement to well-  
 225 known calculations (see, e.g., Schulz and Lanzerotti, 1974).

### 226 2.3 Spatial-energy structure of the CNO group ions fluxes

227 In Figs. 5 and 6 CNO group ions fluxes, averaged for quiet periods ( $K_p < 2$ ), are presented.

228 Figure 5 sums up results from the satellites ATS-6: Applications Technology Satellite 6  
 229 (Spjeldvik and Fritz, 1978; Fritz and Spjeldvik, 1981) and ISEE-1: The International Sun-Earth  
 230 Explorer 1 (Hovestadt et al., 1978). These results have been collected during minimum period  
 231 between 20<sup>th</sup> / 21<sup>th</sup> of the solar activity cycles (1974–1975, 1977).

232 Figure 6 sums up results from the satellite Explorer-45 (Spjeldvik and Fritz, 1978; Fritz and  
 233 Spjeldvik, 1981). These results were obtained during maximum period of activity in 20<sup>th</sup> solar  
 234 cycle (1971–1972).

235 On Figs. 5–6 the spatial-energy patterns of the ion fluxes of the CNO group are even more  
 236 shifted towards higher values of  $L$  shell and its configuration differ significantly from Figs. 1–4.

237 From a comparison of Figs. 1–2 with Figs. 5–6 one can see that, for ions of CNO group, the  
 238 solar-cyclic (11-year) variations are greater than for protons. For example, at  $L \sim 3–5$  from  
 239 maximum to minimum of solar activity fluxes of protons with  $E > 1$  MeV practically do not  
 240 changed, but the fluxes of the CNO group increase by one order of magnitude or more. From a  
 241 comparison of Figs. 3–4 with Figs. 5–6 it is seen also that the fluxes of CNO group change several  
 242 times more than the fluxes of helium ions do.

243 This means that, for ions of the CNO group, the ionization losses at  $L = 3–5$  are much larger  
 244 than for ions with  $Z \leq 2$  and these losses have a significant effect even on the power-law segment  
 245 of the spectra of the CNO ions (in the part which is seen on Figs. 5–6). Therefore, the lower  
 246 boundary of the power-law tail of these ions spectra have not been obtained by the experiments  
 247 collected in Figs. 5 and 6. The red line on these figures corresponds to adiabatic laws (see  
 248 Kovtyukh, 2001); this line let us estimate the deviations from these laws. As can be seen from Fig.  
 249 5–6, ionization losses for ions of the CNO group are especially large at the peak of solar activity  
 250 (Fig. 6): during these times, the slope of iso-lines on  $L > 3$  is significantly less than the slope of the  
 251 red line.

252 At the same time, at  $L > 4$  in Fig. 5 and at  $L > 3$  in Fig. 6, the iso-lines of fluxes pass almost  
 253 parallel to each other and at approximately equal distances from each other; the average value of  $\gamma$   
 254 corresponding to them is  $\sim 6$ . Thus, for sufficiently large values of  $E$  and  $L$ , the CNO group ions  
 255 spectra in the ERB have a power-law form, but these spectra are softer in comparison with the  
 256 spectra of protons.

257 The red line corresponds here to the dependences  $E_b/M_i \approx 43.4 \times L^{-3}$  MeV/n (on Fig. 5) and  $E_b/M_i$   
 258  $\sim 12.4 \times L^{-3}$  MeV/n (on Fig. 6), which are taken from (Kovtyukh, 2001) where this boundary was  
 259 more clearly defined also for the ions of the CNO group. If one takes into account that at  $L \sim 3–5$   
 260 for the CNO group ions with  $E > 0.1$  MeV/n the average charge  $Q_i = +4$  (see, e.g., Spjeldvik and

261 Fritz, 1978), then for this boundary one can get:  $\mu_b \sim 1.4 \times Q_i \text{ keV/n} \times \text{nT}^{-1}$  at the maximum of solar  
 262 activity and  $\mu_b \sim 1.4 \times M_i \text{ keV/n} \times \text{nT}^{-1}$  at the minimum of solar activity (for the dipole magnetic field  
 263 region).

### 264 3 Discussion

265 Let us consider the conclusions following the results obtained here for solar-cyclic variations in the  
 266 fluxes of ERB ions. Solar-cyclic (11-year) variations of proton fluxes with  $E > 1$  MeV in the inner  
 267 region of the ERB have been studied in many works (see, e.g., Pizzella et al., 1962; Hess, 1962;  
 268 Blanchard and Hess, 1964; Filz, 1967; Nakano and Heckman, 1968; Vernov, 1969; Dragt, 1971;  
 269 Huston et al., 1996; Vacaressse et al., 1999; Kuznetsov et al., 2010; Qin et al., 2014). These  
 270 variations reach one order of magnitude at  $L = 1.14$  and are reduced rapidly with increasing  $L$  (see,  
 271 e.g., Vacaressse et al., 1999).

272 In these works, such variations of the proton fluxes of the inner belt are connected to the solar-  
 273 cyclic variations of the energy loss rates of protons in this region. However, solar-cyclic variations  
 274 of fluxes of ions with  $Z \geq 2$  have not been considered in these works.

275 In quiet periods, only the mechanism of ionization loss is significant for the ERB protons  
 276 trapped in small  $L$  shells (see, e.g., Schulz and Lanzerotti, 1974). Energy loss rates and lifetimes of  
 277 the ERB protons are determined, in this mechanism, by the density of atmospheric atoms and  
 278 ionospheric plasma ( $N$ ) in a geomagnetic trap. This density depends on the intensity of the  
 279 ultraviolet radiation of the Sun.

280 With decreasing solar activity (with a transition from maximum to minimum of the solar cycle),  
 281 the densities of atmospheric atoms and ionospheric plasma in a geomagnetic trap are decreased. If  
 282 the proton supply rates to the inner belt, under the action of the CRAND mechanism, remain  
 283 unchanged or the effect of these changes is weaker than the effect connected with changes of loss  
 284 rates of the protons, the stationary proton fluxes will increase with decreasing solar activity.

285 The lifetimes of protons increase with  $L$ ; this leads to a decrease in the amplitude of the solar-  
 286 cyclic variations of proton fluxes. A proton lifetime on a given  $L$  shell depends on its energy and is  
 287 less than 11 years at  $L < L^*(E)$ . For example, for protons with  $E \sim 10$  MeV the value  $L^*$  is  $\sim 2.5$   
 288 (see, e.g., Kovtyukh, 2016a). Figs. 1 and 2 show that for protons the solar-cyclic variations of  
 289 fluxes are small and localized at  $L < 2.5$  (mainly at  $L < 1.4$ ).

290 In contrast to protons, Figs. 3–6 show significant solar-cyclic variations of fluxes of helium ions  
 291 and CNO group ions at  $L \sim 2$ –5. These variations can be explained by the same mechanism, that  
 292 has been suggested for protons at  $L < 2.5$ .

293 For ions with  $Z \geq 2$  in the ERB, ionization losses are more significant than for protons and this  
 294 can be connected to the absence of ions with  $Z \geq 2$  at  $L < 2$  (or very low values of these fluxes)  
 295 during quiet geomagnetic conditions. Such short lifetimes are manifested also in the slope of the  
 296 experimental curves in Fig. 4 and 6 (this was noted in sections 2.2 and 2.3, respectively).  
 297 Consequently, for ions with  $Z \geq 2$ , the regions in which variations can manifested, should be  
 298 located on higher  $L$  shells (at the same energies as for protons).

299 The lifetimes of ions in the energy ranges considered here are  $\tau \propto M_i^{-1/2} Q_i^{-2} N^{-1} E^{3/2}$  (Schulz and  
 300 Lanzerotti, 1974). In a first approximation, for  $N \propto L^{-4}$ , we obtain the value  $L_i^* \sim (M_i^{1/2} Q_i^2)^{1/4} L^*$ ,  
 301 where  $L^*$  corresponds to the  $L$  shell of protons of the same energy of the other ions under study. For  
 302 helium ions ( $M_i = 4$ ,  $Q_i = 2$ ) with  $E \sim 10$  MeV, we obtain  $L_i^* \sim 4.2$ . For ions of CNO group ( $M_i = 14$ ,  
 303  $Q_i = 4$ ) with  $E \sim 10$  MeV we obtain  $L_i^* \sim 6.9$ . These are very rough estimations, but they are in  
 304 agreement with the results presented in Figs. 3–6.

305 These estimates are based on the following assumption: during variations in solar activity, the rates  
 306 of ion supply on  $L < L_i^*$  remains unchanged (or these changes are weaker than the effect of changes of  
 307 the rate of ion losses). This assumption is real for protons with  $E > 10$ –20 MeV at  $L < 2.2$ ; in fact,

308 these protons form mainly under the action of the CRAND mechanism. However, at  $L > 2.2$  the  
309 stationary ion fluxes of the ERB form mainly under the action of radial diffusion (see, e.g., Schulz and  
310 Lanzerotti, 1974; Kovtyukh, 2016b, 2018). Therefore, the solar-cyclic variations of  $Z \geq 2$  ion fluxes  
311 can be motivated only under the assumption that the effect related with an increase in the ionization  
312 losses of such ions significantly exceeds the effect connected with the possible enhance of radial  
313 diffusion of ions during the rising phase of solar activity.

314 In the experimental results presented here for the ERB ions, the region of the power-law tail of  
315 the ion spectra is distinguished. For many experiments, especially for heavy ions, the values of the  
316 parameter of a power-law tail spectra are determined much more accurately by the dependences  
317  $J(L)$  of the ion fluxes (in logarithmic scale) for different pairs of energy channels (see Kovtyukh,  
318 2001). For example, the range of  $L$ , in which these dependences for two energy channels are  
319 parallel to each other is connected to the power-law tail of the spectra. Instead, on smaller values  
320 of  $L$ , these fluxes begin to converge and the radial dependences of these fluxes intersect with each  
321 other, which is related to the maximum in the spectra.

322 The main source of ions in the outer regions of the ERB is the solar wind, and usually the high-  
323 energy part of these spectra have an exponential shape (see, e.g., Ipavich et al., 1981a, 1981b).  
324 Immediately before being captured into the magnetosphere, these ions pass through a highly  
325 turbulized regions, but the high-energy part of their spectra usually retains an exponential shape.  
326 Therefore, the question arises: what physical mechanism converts the form of ion spectra from  
327 exponential to power-law?

328 Evidently, the power-law tail of the ERB ions spectra must be generated-in the outer regions of  
329 the magnetosphere. The most likely region for this to happen is the plasma sheet (PS) of the  
330 magnetospheric tail, which is adjacent to the geomagnetic trap. The high-energy part of the ion  
331 spectra in the PS, at  $R \sim 20\text{--}40 R_E$ , has a power-law shape and the exponents of these spectra are  
332 close to the corresponding parameters of the spectra of ions in the ERB. On the data of the  
333 satellites IMP-7 and IMP-8 (Sarris et al., 1981; Lui et al., 1981) and also satellite ISEE-1 (Christon  
334 et al., 1991), the shape of the ion spectra of the PS usually do not change during substorms; they  
335 produce only parallel shifts of the spectra along logarithmic axes  $E$  and  $J$ . These results point out  
336 that the time scales of formation processes of these ion spectra in the PS exceed the times of  
337 substorms.

338 Parameters of the power-law tail of the ion spectra of the outer belt ( $\gamma$  and  $\mu_b$ ) reflect,  
339 apparently, the most fundamental features of the mechanisms of acceleration of ions in the tail of  
340 the magnetosphere. One can try to connect the values of these parameters with the most general  
341 representations of the mechanisms of ion acceleration in the PS of the magnetospheric tail.

342 Most likely, this part of the ion energy spectra is formed in the PS by stochastic mechanisms of  
343 ion acceleration; this hypothesis is supported by many experimental results. The statistical aspect  
344 of these mechanisms reveals itself, in particular, in the fact that the ratios of fluxes (and partial  
345 densities) of ions with different  $Z$  can differ, even greatly, at low and high energies. During their  
346 wander in the phase space, ions gradually loose information about their origin and, therefore, the  
347 high-energy tails of their spectra contain ambiguous information on the partial densities of  
348 different components of ions in the source (see, e.g., Kovtyukh, 2001).

349 The high-energy part of the ion spectra of the PS can be generated by the mechanisms of  
350 acceleration of particles on magnetic irregularities moving with respect to each other (Fermi  
351 mechanism). The fractal structures of the PS are revealed on scales from  $\sim 0.4$  to  $\sim 8$  thousands  
352 kilometers, for example, in the data of the satellite Geotail (Milovanov et al., 1996). If the mass of  
353 the ions are small compared to the mass of the magnetic irregularities in the PS, the average values  
354 of the index  $\gamma$  of the power-law tail should not depend on mass and charge of such nuclei.

355 Under equilibrium conditions, this parameter is determined by the average part of energetic ions  
356 in the total energy density of particles and magnetic irregularities ( $\bar{\beta}$ ). From the theory which was  
357 developed by Ginzburg and Syrovatskii (1964), it follows:  $\gamma - 1 \approx (1 - \bar{\beta})^{-1}$ . With increasing  $\bar{\beta}$  in



358 the interval  $0 < \bar{\beta} < 1$ , the value  $\gamma$  increases monotonically and  $\gamma \rightarrow \infty$  for  $\bar{\beta} \rightarrow 1$ . For real  
359 average values  $\bar{\beta}$  in the central PS, we get  $\gamma \sim 3.5-7.0$  ( $\gamma \sim 4.3$  at  $\bar{\beta} \sim 0.7$ ).

360 Spectra with power-law tail and quasi-exponential segment at lower energies can be generated  
361 when the value  $\Delta B/\bar{B}$  for magnetic irregularities is proportional to their size  $\delta r$  and their spectral  
362 density decreases rapidly with increasing  $\delta r$  for  $\delta r < r_s$ , but for  $\delta r > r_s$  it remains almost  
363 unchanged. Apparently, the spectra of magnetic irregularities in PS with thickness  $r_s$  have just such  
364 form. Then, the lower boundary  $\mu_b$  of the power-law tail corresponds to the condition  $r_s/\rho_i \sim 10$  ( $\rho_i$   
365 is the gyroradius of ions), i.e.  $\mu_b \sim 0.02(Q_i^2/M_i)B_s r_s^2$  keV nT<sup>-1</sup>, where  $B_s$  is the average magnetic  
366 field induction in the PS (in nT) and  $r_s$  is normalized to the Earth's radius. Using  $B_s \sim 30$  nT and  $r_s$   
367  $\sim 1.3 R_E$  it can be obtained:  $\mu_b \sim 1.0 (Q_i^2/M_i)$  keV nT<sup>-1</sup>.

368 The energy spectra of ions in the radiation belts of such planets as Jupiter and Saturn have the  
369 form analogous to that of ion spectra in the ERB (see, e.g., Krimigis et al., 1981; Cheng et al.,  
370 1985). As that in the ERB, these spectra have a long power-law tail, which is formed, apparently,  
371 by mechanisms of stochastic acceleration of ions as a result of their interactions with the current  
372 layer of the magnetospheric tail.

## 373 5 Conclusions

374 In this work, the experimental results for the stationary fluxes of the main ion components of the  
375 ERB (protons, helium ions and ions of the CNO group) in the near equatorial plane, have been  
376 analyzed. It has been found that in the outer belt these fluxes line up in the certain regular  
377 patterns in the space  $\{E, L\}$ . The degree of such similarity increases with increasing  $E$  and  $L$  and it  
378 is linked to the nature of the main sources and on the universality mechanisms of transfer,  
379 acceleration and losses of ERB ions in the outer belt (radial diffusion which conserves  $\mu$  and  $K$  of  
380 ions, betatron acceleration and ionization losses).

381 Moreover, solar-cyclic (11-year) variations of the spatial-energy distributions of the ERB ion  
382 fluxes have been investigated. It has been noted that the ERB ions fluxes are weaker with  
383 increasing solar activity and this effect increases with increasing atomic number  $Z$ . This kind of  
384 dependence of the amplitude of flux changes on  $Z$  is typical, also, for faster variations in the fluxes  
385 of the ERB ions, during geomagnetic storms and other disturbances of the Earth's magnetosphere,  
386 as has been underlined in the review Kovtyukh (2018).

387 The figures presented here make it possible to determine in which regions of the space  $\{E, L\}$   
388 near the equatorial plane the ionization losses of ions during their radial diffusion can be neglected  
389 and where this cannot. These results indicate also that with variations in the level of solar activity  
390 the coefficient  $D_{LL}$  of the radial diffusion of the ERB ions change much less than the ionization  
391 losses rates of ions with  $Z \geq 2$ .

392 In addition, the figures given here reveal the localization of "white spots", especially extensive for  
393 ions with  $Z \geq 2$  and  $E > 1$  MeV/n at  $L < 3$ . As  $Z$  and energy become larger and  $L$  becomes smaller,  
394 the uncertainties in the values of the ERB fluxes become larger. These gaps must be filled by the  
395 results of future experiments on satellites; for now, the extensive gaps in  $Z \geq 2$  ion data do not allow  
396 to create sufficiently complete and reliable empirical models of the ERB for these ions.

397

398 **Acknowledgements.** The author are very grateful to the reviewers for their very important and  
399 fruitful comments and proposals for the paper.

400 **Financial support.** This work was supported by Russian Foundation for Basic Research RFFI  
401 grant No. 17-29-01022.

## 402 References

403 Alfvén, H., and Fälthammar, C.-G.: *Cosmical Electrodynamics, Fundamental Principles*,  
404 Clarendon Press, Oxford, 1963.

405 Albert, J. M., Ginet, G. P., and Gussenhoven, M. S.: CRRES observations of radiation belt protons,  
406 1, Data overview and steady state radial diffusion, *J. Geophys. Res.*, **103**(A5), 9261–9273.  
407 <https://doi.org/10.1029/97JA02869>, 1998.

408 Blake, J. B., and Fennell, J. F.: Heavy ion measurements in the synchronous altitude region, *Planet.*  
409 *Space Sci.*, **29**(11), 1205–1213, [https://doi.org/10.1016/0032.0633\(81\)90125-2](https://doi.org/10.1016/0032.0633(81)90125-2), 1981.

410 Blake, J. B., Fennell, J. F., Schulz, M., and Paulikas, G. A.: Geomagnetically trapped alpha  
411 particles, 2, The inner zone, *J. Geophys. Res.*, **78**(25), 5498–5506,  
412 <https://doi.org/10.1029/JA078i025p05498>, 1973.

413 Blanchard, R. C., and Hess, W. N.: Solar cycle changes in inner-zone protons, *J. Geophys. Res.*,  
414 **69**(19), 3927–3938, <https://doi.org/10.1029/JZ069i019p03927>, 1964.

415 Chenette, D. L., Blake, J. B., and Fennell, J. F.: The charge state composition of 0.4–MeV helium  
416 ions in the Earth’s outer radiation belts during quiet times, *J. Geophys. Res.*, **89**(A9), 7551–  
417 7555, <https://doi.org/10.1029/JA089iA09p07551>, 1984.

418 Cheng, A. F., Krimigis, S. M., and Armstrong, T. P.: Near equality of ion phase space densities at  
419 Earth, Jupiter, and Saturn, *J. Geophys. Res.*, **90**(A9), 526–530,  
420 <http://doi.org/10.1029/JA090iA01p00526>, 1985.

421 Christon, S. P., Williams, D. J., Mitchell, D. G., Huang, C. Y., and Frank, L. A.: Spectral  
422 characteristics of plasma sheet ion and electron populations during disturbed geomagnetic  
423 conditions, *J. Geophys. Res.*, **96**(A1), 1–22, <https://doi.org/10.1029/90JA01633>, 1991.

424 Croley, D. R., Jr., Schulz, M., and Blake, J. B.: Radial diffusion of inner-zone protons:  
425 Observations and variational analysis, *J. Geophys. Res.*, **81**(4), 585–594,  
426 <https://doi.org/10.1029/JA081i004p00585>, 1976.

427 Dragt, A. J.: Solar cycle modulation of the radiation belt proton flux, *J. Geophys. Res.*, **76**(10),  
428 2313–2344, <https://doi.org/10.1029/JA076i010p02313>, 1971.

429 Fennell, J. F., and Blake, J. B.: Geomagnetically trapped  $\alpha$ -particles, *Magnetospheric Particles and*  
430 *Fields*, edited by: McCormac, B. M., D. Reidel, Dordrecht, Holland, 149–156, 1976.

431 Filz, R. C.: Comparison of the low-altitude inner-zone 55–MeV trapped proton fluxes measured in  
432 1965 and 1961–1962, *J. Geophys. Res.*, **72**(3), 959–963,  
433 <https://doi.org/10.1029/JZ072i003p00959>, 1967.

434 Freden, S. C., Blake, J. B., and Paulikas, G. A.: Spatial variation of the inner zone trapped proton  
435 spectrum, *J. Geophys. Res.*, **70**(13), 3113–3116, <https://doi.org/10.1029/JZ070i013p03113>,  
436 1965.

437 Fritz, T. A., and Spjeldvik, W. N.: Observations of energetic radiation belt helium ions at the  
438 geomagnetic equator during quiet conditions, *J. Geophys. Res.*, **83**(A6), 2579–2583,  
439 <https://doi.org/10.1029/JA083iA06p02579>, 1978.

440 Fritz, T. A., and Spjeldvik, W. N.: Simultaneous quiet time observations of energetic radiation belt  
441 protons and helium ions: The equatorial  $\alpha/p$  ratio near 1 MeV, *J. Geophys. Res.*, **84**(A6),  
442 2608–2618, <https://doi.org/10.1029/JA084iA06p02608>, 1979.

443 Fritz, T. A., and Spjeldvik, W. N.: Steady-state observations of geomagnetically trapped energetic  
444 heavy ions and their implications for theory, *Planet. Space Sci.*, **29**(11), 1169–1193,  
445 [https://doi.org/10.1016/0032-0633\(81\)90123-9](https://doi.org/10.1016/0032-0633(81)90123-9), 1981.

446 Ginzburg, V. L., and Syrovatskii, S. I.: *The Origin of Cosmic Rays*, Pergamon Press, Oxford,  
447 1964.

448 Ginet, G. P., O’Brien, T. P., Huston, S. L., Johnston, W. R., Guild, T. B., Friedel, R., Lindstrom,  
449 C. D., Roth, C. J., Whelan, P., Quinn, R. A., Madden, D., Morley, S., and Su, Yi-J.: AE9, AP9  
450 and SPM: New models for specifying the trapped energetic particle and space plasma  
451 environment, *Space Sci. Rev.*, **179**(1–4), 579–615, <https://doi.org/10.1007/s11214-013-9964-y>,  
452 2013.

453 Goka, T., Matsumoto, H., and Takagi, S.: Empirical model based on the measurements of the  
454 Japanese spacecrafts, *Radiation Measurements*, **30**(5), 617–624, [https://doi.org/10.1016/S1350-](https://doi.org/10.1016/S1350-4487(99)00237-1)  
455 [4487\(99\)00237-1](https://doi.org/10.1016/S1350-4487(99)00237-1), 1999.

456 Hess, W. N.: Discussion of paper by Pizzella, McIlwain, and Van Allen, ‘Time variations of  
457 intensity in the Earth’s inner radiation zone, October 1959 through December 1960’, *J.*  
458 *Geophys. Res.*, **67**(12), 4886–4887, <https://doi.org/10.1029/JZ0670i012p04886>, 1962.

459 Hovestadt, D., Häusler, B., and Scholer, M.: Observation of energetic particles at very low  
460 altitudes near the geomagnetic equator, *Phys. Rev. Lett.*, **28**(20), 1340–1343,  
461 <https://doi.org/10.1103/PhysRevLett.28.1340>, 1972.

462 Hovestadt, D., Gloeckler, G., Fan, C. Y., Fisk, L. A., Ipavich, F.M., Klecker, B., O’Gallagher, J. J.,  
463 and Scholer, M.: Evidence for solar wind origin of energetic heavy ions in the Earth’s radiation  
464 belt, *Geophys. Res. Lett.*, **5**(12), 1055–1057, <https://doi.org/10.1029/GL005i012p01055>, 1978.

465 Hovestadt, D., Klecker, B., Mitchell, E., Fennell, J. F., Gloeckler, G., and Fan, C. Y.: Spatial  
466 distribution of  $Z \geq 2$  ions in the outer radiation belt during quiet conditions, *Adv. Space Res.*,  
467 **1**(1), 305–308, [https://doi.org/10.1016/0273-1177\(81\)90125-3](https://doi.org/10.1016/0273-1177(81)90125-3), 1981.

468 Huston, S., Kuck, G., and Pfitzer, K.: Low-altitude trapped radiation model using TIROS/NOAA  
469 data, *Radiation Belts: Models and Standards*, edited by: Lemaire, J. F., Heynderickx, D., and  
470 Baker, D. N., AGU, Washington, D. C., 119–122, <https://doi.org/10.1029/GM097/p0119>, 1996.

471 Ilyin, B. D., Kuznetsov, S. N., Panasyuk, M. I., and Sosnovets, E.N.: Non-adiabatic effects and  
472 boundary of the trapped protons in the Earth's radiation belts, *Bulletin of the Russian Academy*  
473 *of Sciences: Physics*, **48**(11), 2200–2203, 1984.

474 Ipavich, F. M., Galvin, A. B., Gloeckler, G., Scholer, M., and Hovestadt D.: A statistical survey of  
475 ions observed upstream of the Earth’s bow shock: Energy spectra, composition, and spatial  
476 variation, *J. Geophys. Res.*, **86**(A6), 4337–4342, <https://doi.org/10.1029/JA086iA06p4337>,  
477 1981a.

478 Ipavich, F. M., Scholer, M., and Gloeckler, G.: Temporal development of composition, spectra,  
479 and anisotropies during upstream particle events, *J. Geophys. Res.*, **86**(A13), 11153–11160,  
480 <https://doi.org/10.1029/JA086iA13p11153>, 1981b.

481 Kovtyukh, A. S.: Geocorona of hot plasma, *Cosmic Res.*, **39**(6), 527–558,  
482 <https://doi.org/10.1023/A:1013074126604>, 2001.

483 Kovtyukh, A. S.: Radial dependence of ionization losses of protons of the Earth’s radiation belts,  
484 *Ann. Geophys.*, **34**(1), 17–28, <https://doi.org/10.5194/angeo-34-17-2016>, 2016a.

485 Kovtyukh, A. S.: Deduction of the rates of radial diffusion of protons from the structure of the  
486 Earth’s radiation belts, *Ann. Geophys.*, **34**(11), 1085–1098. [https://doi.org/10.5194/angeo-34-1085-](https://doi.org/10.5194/angeo-34-1085-2016)  
487 [2016](https://doi.org/10.5194/angeo-34-1085-2016), 2016b.

488 Kovtyukh, A. S.: Ion Composition of the Earth’s Radiation Belts in the Range from 100 keV to  
489 100 MeV/nucleon: Fifty Years of Research, *Space Sci. Rev.*, **214**(8), 124:1–124:30,  
490 <https://doi.org/10.1007/s11214-018-0560-z>, 2018.

491 Krimigis, S. M.: Alpha particles trapped in the Earth's magnetic field, *Particles and Fields in the*  
492 *Magnetosphere*, edited by: McCormac, B. M., D. Reidel, Dordrecht, Holland, 364–379, 1970.

493 Krimigis, S. M., Carbary, J. F., Keath, E. P., Bostrom, C. O., Axford, W. I., Gloeckler, G.,  
494 Lanzerotti, L. J., and Armstrong, T. P.: Characteristics of hot plasma in the Jovian  
495 magnetosphere: Results from the Voyager spacecraft, *J. Geophys. Res.*, **86**(A10), 8227–8257.  
496 <http://doi.org/10.1029/JA086iA10p08227>, 1981.

497 Kuznetsov, N. V., Nikolaeva, N. I., and Panasyuk, M. I.: Variation of the trapped proton flux in the  
498 inner radiation belt of the Earth as a function of solar activity, *Cosmic Res.*, **48**(1), 80–85,  
499 <https://doi.org/10.1134/S0010952510010065>, 2010.

500 Lui, A. T. Y., and Krimigis, S. M.: Several features of the earthward and tailward streaming of  
501 energetic protons (0.29–0.5 MeV) in the Earth's plasma sheet, *J. Geophys. Res.*, **86**(A13),  
502 [11173–11188](https://doi.org/10.1029/JA086iA13p11173), <https://doi.org/10.1029/JA086iA13p11173>, 1981.

- 503 Lutsenko, V. N., and Nikolaeva, N. S.: Relative content and the range of alpha particles in the  
504 inner radiation belt of the Earth by measurements on satellite Prognoz-5, *Cosmic Res.*, **16**(3),  
505 459–462, 1978.
- 506 McIlwain, C. E.: Coordinate for mapping the distribution of magnetically trapped particles, *J.*  
507 *Geophys. Res.*, **66**(11), 3681–3691, <https://doi.org/10.1029/JZ066i011p03681>, 1961.
- 508 Milovanov, A. V., Zelenyi, L. M., and Zimbardo, G.: Fractal structures and power low spectra in  
509 the distant Earth's magnetotail, *J. Geophys. Res. Space Phys.*, **101**(A9), 19903–19910,  
510 <https://doi.org/10.1029/96JA01562>, 1996.
- 511 Nakano, G., and Heckman, H.: Evidence for solar-cycle changes in the inner-belt protons, *Phys.*  
512 *Rev. Lett.*, **20**(15), 806–809, <https://doi.org/10.1103/PhysRevLett.20.806>, 1968.
- 513 Northrop, T. G.: *The Adiabatic Motion of Charged Particles*, Wiley-Interscience, NY, USA, 1963.
- 514 Panasyuk, M. I., and Sosnovets, E. N.: Differential energy spectrum of low-energy protons in the  
515 inner region of the radiation belt, *Cosmic Res.*, **11**(3), 436–440, 1973.
- 516 Panasyuk, M. I., Reizman, S. Ya., Sosnovets, E. N., and Filatov, V. N.: Experimental results of  
517 protons and  $\alpha$ -particles measurements with energy more 1 MeV/nucleon in the radiation belts,  
518 *Cosmic Res.*, **15**(6), 887–894, 1977.
- 519 Pizzella, G., McIlwain, C. E., and Van Allen, J. A.: Time variations of intensity in the Earth's  
520 inner radiation zone, October 1959 through December 1960, *J. Geophys. Res.*, **67**(4), 1235–  
521 1253, <https://doi.org/10.1029/JZ0670i004p01235>, 1962.
- 522 Pizzella, G., and Randall, B. A.: Differential energy spectrum of geomagnetically trapped protons  
523 with the Injun 5 satellite, *J. Geophys. Res.*, **76**(10), 2306–2312,  
524 <https://doi.org/10.1029/JA076i010p02306>, 1971.
- 525 Qin, M., Zhang, X., Ni, B., Song, H., Zou, H., and Sun, Y.: Solar cycle variations of trapped  
526 proton flux in the inner radiation belt, *J. Geophys. Res. Space Phys.*, **119**(12), 9658–9669,  
527 <https://doi.org/10.1002/2014JA020300>, 2014.
- 528 Sarris, E. T., Krimigis, S. M., Lui, A. T. Y., Ackerson, K. L., Frank, L. A., and Williams, D. J.:  
529 Relationship between energetic particles and plasmas in the distant plasma sheet, *Geophys. Res.*  
530 *Lett.*, **8**(4), 349–352, <https://doi.org/10.1029/GL008i004p0349>, 1981.
- 531 Schulz, M., and Lanzerotti, L. J.: *Particle Diffusion in the Radiation Belts*, Springer, NY, USA,  
532 1974.
- 533 Selesnick, R. S., Hudson, M. K., and Kress, B. T.: Injection and loss of inner radiation belt protons  
534 during solar proton events and magnetic storms, *J. Geophys. Res. Space Phys.*, **115**(A8),  
535 A08211, <https://doi.org/10.1029/2010JA015247>, 2010.
- 536 Selesnick, R. S., Baker, D. N., Jaynes, A. N., Li, X., Kanekal, S. G., Hudson, M. K., and Kress, B.  
537 T.: Observations of the inner radiation belt: CRAND and trapped solar protons, *J. Geophys.*  
538 *Res. Space Phys.*, **119**(8), 6541–6552, <https://doi.org/10.1002/2014JA020188>, 2014.
- 539 Selesnick, R. S., Baker, D. N., Kanekal, S. G., Hoxie, V. C., and Li, X.: Modeling the proton  
540 radiation belt with Van Allen Probes Relativistic Electron-Proton Telescope data, *J. Geophys.*  
541 *Res. Space Phys.*, **123**(1), 685–697, <https://doi.org/10.1002/2017JA024661>, 2018.
- 542 Spjeldvik, W. N.: Expected charge states of energetic ions in the magnetosphere, *Space Sci. Rev.*,  
543 **23**(3), 499–538, <https://doi.org/10.1007/BF00172252>, 1979.
- 544 Spjeldvik, W. N., and Fritz, T. A.: Quiet time observations of equatorially trapped  
545 megaelectronvolt radiation belt ions with nuclear charge  $Z \geq 4$ , *J. Geophys. Res.*, **83**(A9), 4401–  
546 4405, <https://doi.org/10.1029/JA083iA09p04401>, 1978.
- 547 Spjeldvik, W. N., and Fritz, T. A.: Observations of energetic helium ions in the Earth's radiation  
548 belts during a sequence of geomagnetic storms, *J. Geophys. Res.*, **86**(A4), 2317–2328,  
549 <https://doi.org/10.1029/JA086iA04p02317>, 1981.
- 550 Stevens, J. R., Martina, E. F., and White, R. S.: Proton energy distributions from 0.060 to 3.3 MeV  
551 at 6.6 Earth radii, *J. Geophys. Res.*, **75**(28), 5373–5385,  
552 <https://doi.org/10.1029/JA075i028p05373>, 1970.
- 553 Vacaresse, A., Boscher, D., Bourdarie, S., Blanc, M., and Sauvaud, J. A.: Modeling the high-

554 energy proton belt, *J. Geophys. Res. Space Phys.*, **104**(A12), 28601–28613,  
555 <https://doi.org/10.1029/1999JA900411>, 1999.

556 Venkatesan, D., and Krimigis, S. M.: Observations of low-energy (0.3– to 1.8-MeV) differential  
557 spectrums of trapped protons, *J. Geophys. Res.*, **76**(31), 7618–7631,  
558 <https://doi.org/10.1029/JA076i031p07618>, 1971.

559 Vernov, S. N.: The Earth's radiation belts. In G. Bozóki, E. Gombosi, A. Sebestyén, A. Somogyi  
560 (Eds.), *Proc. 11<sup>th</sup> ICRC, Budapest*, 85–162, 1969.

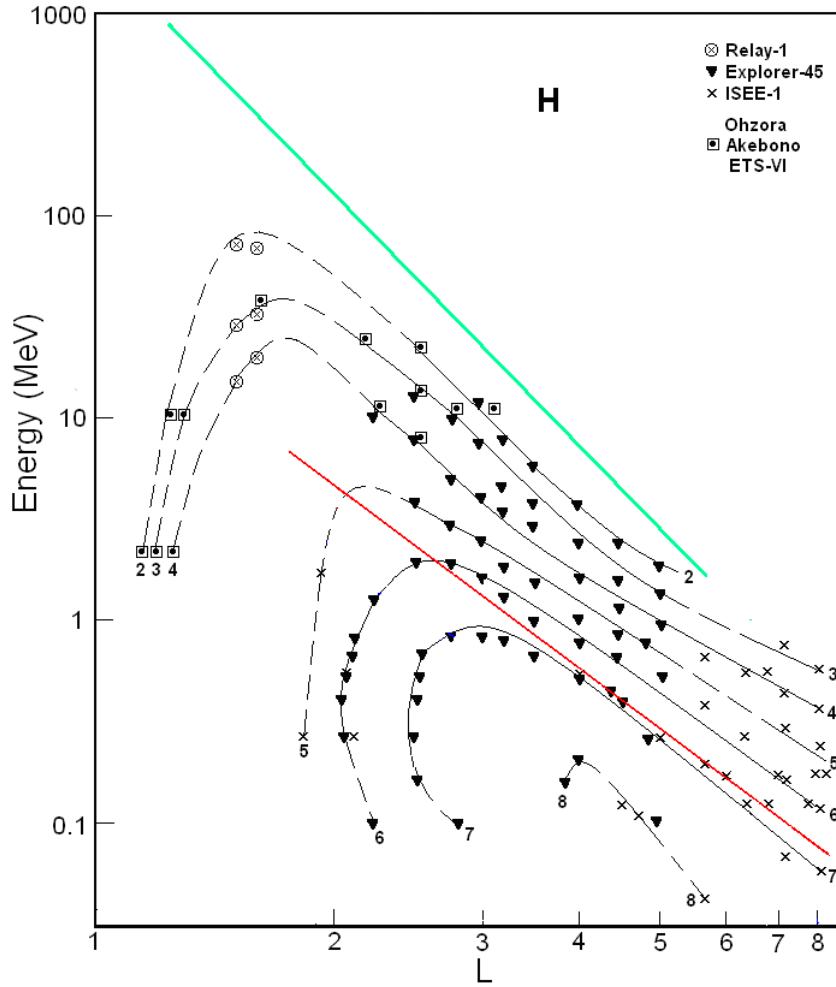
561 Westphalen, H., and Spjeldvik, W.N.: On the energy dependence of the radial diffusion coefficient  
562 and spectra of inner radiation belt particles: Analytic solution and comparison with numerical  
563 results, *J. Geophys. Res.*, **87**(A10), 8321–8326, <https://doi.org/10.1029/2000JA087iA10p08321>,  
564 1982.

565 Wilken, B., Baker, D. N., Highbie, P. R., Fritz, T. A., Olson, W. P., and Pfizter, K. A.:  
566 Magnetospheric configuration and energetic particle effects associated with a SSC: A case study  
567 of the CDAW 6 event on March 22, 1979, *J. Geophys. Res.*, **91**(A2), 1459–1473,  
568 <https://doi.org/10.1029/JA091iA02p01459>, 1986.

569 Williams, D. J.: Phase space variations of near equatorially mirroring ring current ions, *J. Geophys.*  
570 *Res.*, **86**(A1), 189–194, <https://doi.org/10.1029/JA086iA01p00189>, 1981.

571 Williams, D. J., and Frank, L. A.: Intense low-energy ion populations at low equatorial altitude, *J.*  
572 *Geophys. Res.*, **89**(A6), 3903–3911, <https://doi.org/10.1029/JA089iA06p03903>, 1984.

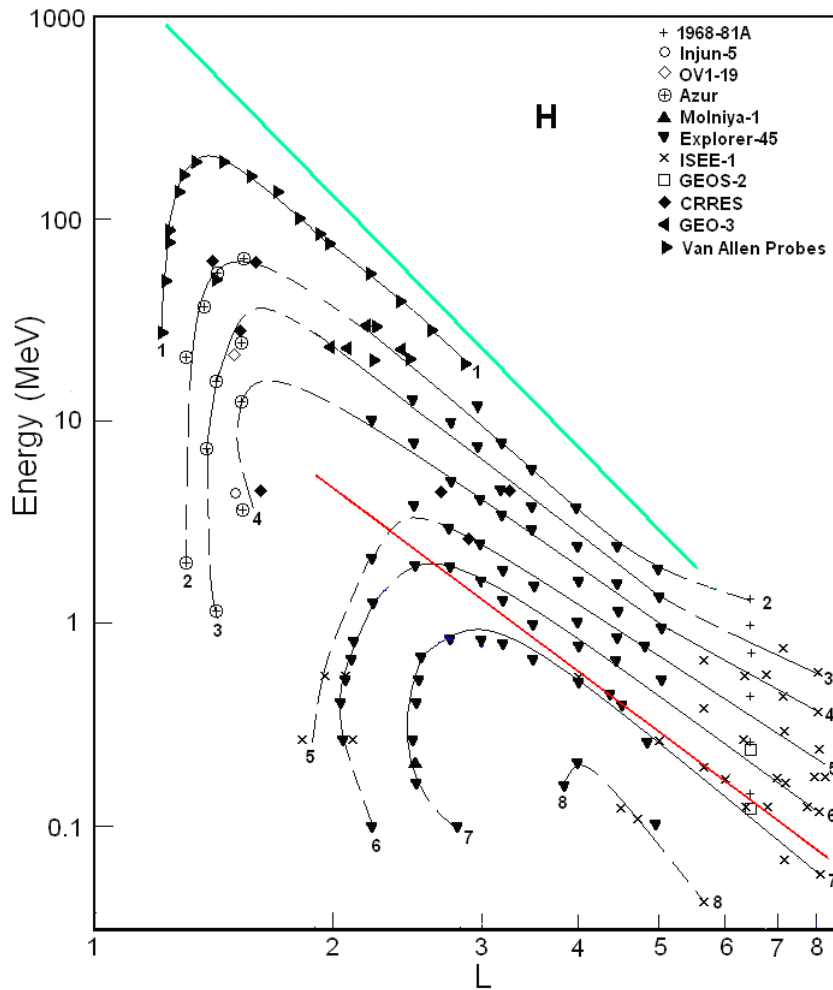
573



574

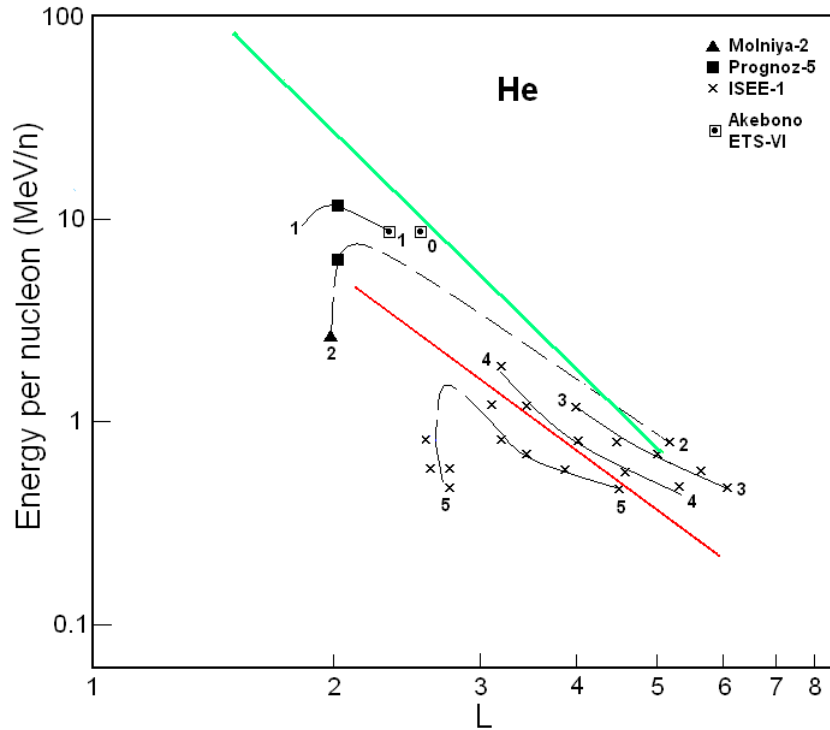
575

576 **Figure 1.** Proton fluxes in the ERB near minima of the solar activity. The numbers on the curves refer to the values of  
 577 the decimal logarithms of  $J$ , which is given in units of  $(\text{cm}^2 \text{ s ster MeV})^{-1}$ , is the differential fluxes of protons with  $\alpha_0 \approx$   
 578  $90^\circ$  (near the plane of the geomagnetic equator). Data of satellites are associated with different symbols. The red line  
 579 corresponds to the lower boundary of the power-law tail of the proton spectra; while green line corresponds to the  
 maximum energy of protons trapped in the ERB (Ilyin et al., 1984).



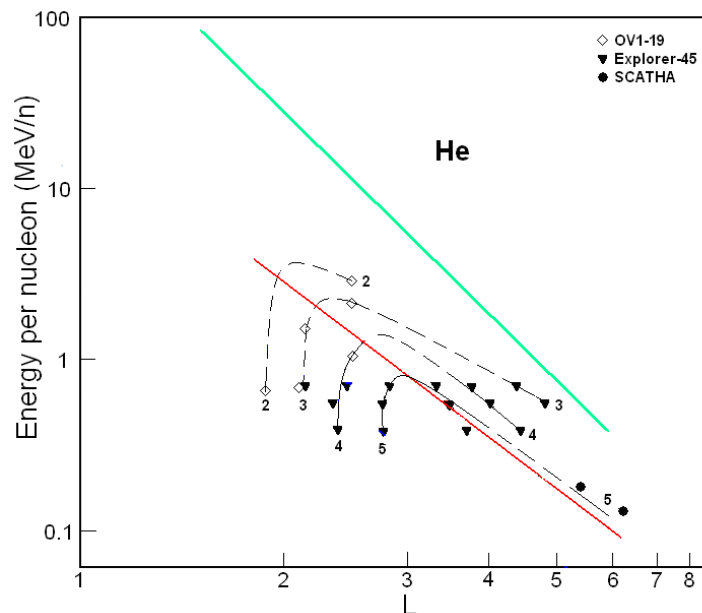
580  
581  
582  
583  
584  
585

**Figure 2.** Proton fluxes in the ERB near maxima of the solar activity. The numbers on the curves refer to the values of the decimal logarithms of  $J$ , which is given in units of  $(\text{cm}^2 \text{ s ster MeV})^{-1}$ , is the differential fluxes of protons with  $\alpha_0 \approx 90^\circ$  (near the plane of the geomagnetic equator). Data of satellites are associated with different symbols. The red line corresponds to the lower boundary of the power-law tail of the proton spectra; while green line corresponds to the maximum energy of protons trapped in the ERB (Ilyin et al., 1984).



586  
587  
588  
589  
590  
591

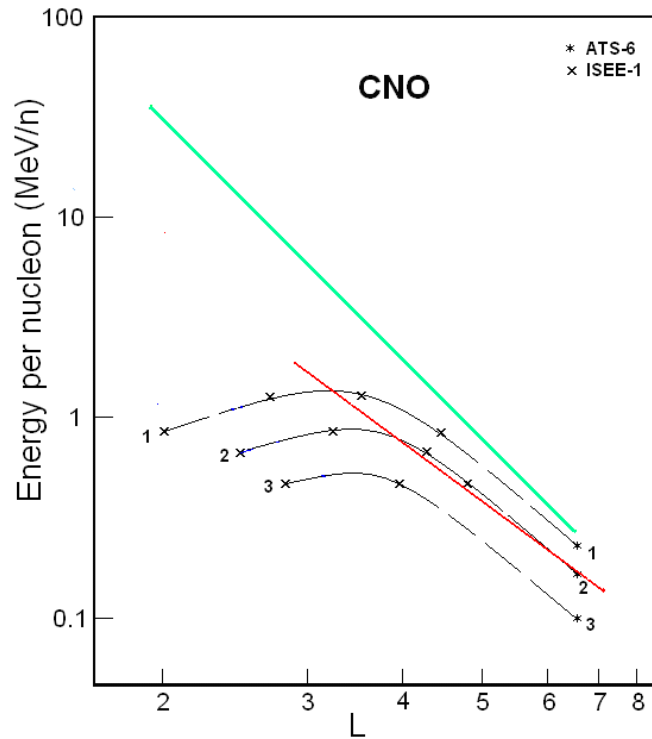
**Figure 3.** Helium ion fluxes in the ERB near minima of the solar activity. The numbers on the curves refer to the values of the decimal logarithms of  $J$ , which is given in units of  $(\text{cm}^2 \text{ s ster MeV/n})^{-1}$ , is the differential fluxes of helium ions with  $\alpha_0 \approx 90^\circ$  (near the plane of the geomagnetic equator). Data of satellites are associated with different symbols. The red line corresponds to the lower boundary of the power-law tail of the helium spectra; while green line corresponds to the maximum energy of these ions trapped in the ERB (Ilyin et al., 1984).



592  
593  
594  
595  
596  
597

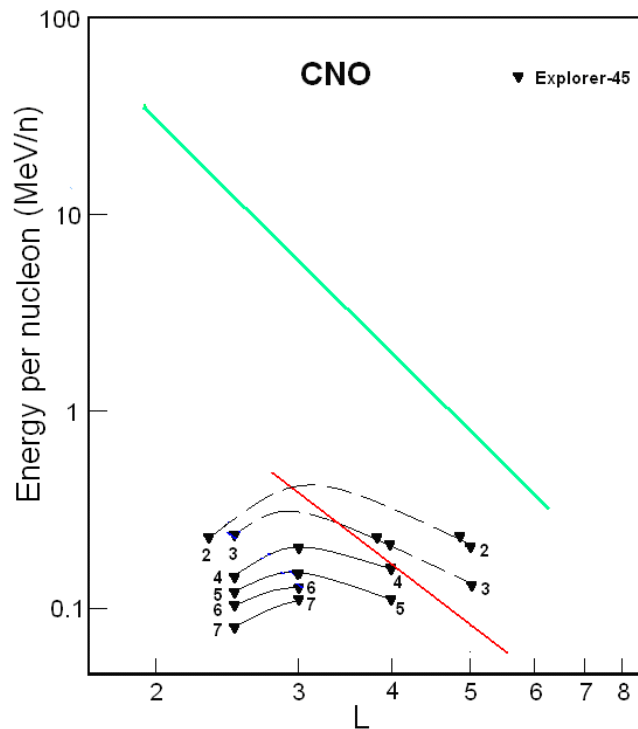
**Figure 4.** Helium ion fluxes in the ERB near maxima of the solar activity. The numbers on the curves refer to the value of the decimal logarithms of  $J$  which is given in units of  $(\text{cm}^2 \text{ s ster MeV/n})^{-1}$ , is the differential fluxes of ions with  $\alpha_0 \approx 90^\circ$  (near the plane of the geomagnetic equator). Data of satellites are associated with different symbols. The red line corresponds to the lower boundary of the power-law tail of the helium spectra; while green line corresponds to the maximum energy of these ions trapped in the ERB (Ilyin et al., 1984).





598  
599  
600  
601  
602  
603

**Figure 5.** CNO ion fluxes in the ERB near minima of the solar activity. The numbers on the curves refer to the values of the decimal logarithms of  $J$ , which is given in units of  $(\text{cm}^2 \text{ s ster MeV/n})^{-1}$ , is the differential fluxes of ions with  $\alpha_0 \approx 90^\circ$  (near the plane of the geomagnetic equator). Data of satellites are associated with different symbols. The red line corresponds to the lower boundary of the power-law tail of the CNO ion spectra; while green line corresponds to the maximum energy of these ions trapped in the ERB (Ilyin et al., 1984).



604  
605  
606  
607  
608  
609

**Figure 6.** CNO ion fluxes in the ERB near the maximum of the solar activity. The numbers on the curves refer to the values of the decimal logarithms of  $J$ , which is given in units of  $(\text{cm}^2 \text{ s ster MeV/n})^{-1}$ , is the differential fluxes of ions with  $\alpha_0 \approx 90^\circ$  (near the plane of the geomagnetic equator). Data of satellites are associated with different symbols. The red line corresponds to the lower boundary of the power-law tail of the CNO ion spectra; while green line corresponds to the maximum energy of these ions trapped in the ERB (Ilyin et al., 1984).